Intact metal/metal halide van der Waals junction enables reliable memristive switching with high endurance

Joo-Hong Lee
Sungkyunkwan University
June-Mo Yang
Sungkyunkwan University
So-Yeon Kim
Sungkyunkwan University
Sungpyo Baek
Sungkyunkwan University
Sungjoo Lee
Sungkyunkwan University
Sung-Joon Lee
University of California Los Angeles https://orcid.org/0000-0003-2368-4647
Nam-Gyu Park
Sungkyunkwan University https://orcid.org/0000-0003-2368-6300
Jin-Wook Lee (jwlee870217@gmail.com)
Sungkyunkwan University https://orcid.org/0000-0002-0170-8620

Article

Keywords: metal halide materials, resistive switching materials, a van der Waals metal contacts

Posted Date: November 23rd, 2021

DOI: https://doi.org/10.21203/rs.3.rs-934133/v1

Intact metal/metal halide van der Waals junction enables reliable memristive switching with high endurance

Joo-Hong Lee[1,†], June-Mo Yang[2,†], So-Yeon Kim[2], Sungpyo Baek[1], Sungjoo Lee[1], Sung-Joon Lee[3,*], Nam-Gyu Park[2,*], Jin-Wook Lee[1,*]

[1]SKKU Advanced Institute of Nanotechnology (SAINT) and Department of Nanoengineering, Sungkyunkwan University, Suwon 16419, Republic of Korea.

[2]School of Chemical Engineering, Sungkyunkwan University, Suwon 16419, Republic o

f Korea.

[3]U.S. Naval Research Laboratory, Washington, DC 20375, United States.

[†]These authors contributed equally to this work.

***Corresponding authors:**

S.-J.L. email: sungjoon.lee.ctr.ks@nrl.navy.mil

N.-G.P. email: npark@skku.edu

J-W.L. email: jw.lee@skku.edu

Organic-inorganic or inorganic metal halide materials have emerged as a promising candidate for a resistive switching material owing to its capability to achieve low operating voltage, high on/off ratio and multi-level switching. However, the high switching variation, limited endurance and poor reproducibility of the device hinder practical use of the memristors. Here, we report a universal approach to relieve the issues by using a van der Waals metal contacts (vdWC). By transferring the pre-deposited metal contact onto the active layers, an intact junction between the metal halide and contact layer is formed without unintended damage in the active layer that has been caused by a conventional physical deposition process of the metal contacts. Compared to the thermally evaporated metal contact (EVC), the vdWC did not degrade optoelectronic quality of the underlying layer to enable memristors with reduced switching variation, significantly enhanced endurance and reproducibility relative to those based on the EVC. By adopting various metal halide active layers, versatile utility of the vdWC is demonstrated. Thus, this vdWC approach can be a useful platform technology for development of high-performance and reliable memristors for future computing.

A memristor has been suggested as a next-generation non-volatile memory and artificial synapses for neuromorphic computing because of desirable scalability and power consumption[1-4]. Various materials including silicon, metal oxides and organics, have been extensively studied as an active layer material for the memristors[3,5,6]. In recent years, organic-inorganic or inorganic metal halide materials have emerged as a promising candidate owing to its ability to achieve high on/off ratio with multilevel storage capability[7], millivolt-scale low operating voltage[7,8], long retention time[9], and mechanical flexibility[10]. Despite these merits, the high switching variation, limited endurance and poor device reproducibility still hinder practical use of the memristors[11].

The low operating voltage of the metal halide based memristors might be originated from relatively fragile chemical bonding constituting the metal halide materials. For example, the bonding dissociation energies for metal-halide bonds such as Pb-I, Pb-Br and Pb-Cl are 1.98, 2.56 and 3.12 eV[12], respectively. These are much lower than those for metal-oxide bonds such as Hf-O (8.26 eV), Mo-O (5.41 eV), Ta-O (8.19 eV) and TiO (6.87 eV)[13-16]. The weaker chemical bonding of the metal halide materials enables generation and migration of ionic defects for formation of conducting filaments (CFs) at a relatively lower operating voltage. However, the weak chemical bonding makes

crystal lattice vulnerable to undesired physical and chemical reactions during fabrication and operation of the device.[17,18] For example, the typical memristors adopt the structure of metal/active material/metal, where the top metal contact is deposited on the active layer through physical deposition processes such as thermal or electron-beam evaporation. In this case, the physical deposition processes involve high-energy metal atom bombardment of the active material film surface, which can cause formation of unintended defects, chemical bonding, and secondary phases[19-21]. Compared to rigid silicon or metal oxides, such damage is supposed to be worsen with the fragile and reactive crystal lattice of the metal halides. The unwanted physical and chemical interaction of the metal contacts with the underlying metal halide layer might hinder formation of a reproducible, clean and uniform junction at the interface[22,23] and thus reliable operation of the memristor devices. However, the side effect caused by the deposition process has been barely considered for the metal halide memristors. More importantly, it is urgently necessary to develop a method to fabricate an intact junction between the metal contact and active layers for future development.

Here, we report van der Waals metal contact (vdWC) approach to form an intact junction between metal contact and underlying metal halide active layer. The vdWC is formed by transferring the pre-deposited metal contact onto the active layer. The vdWC retained high optoelectronic quality of the underlying active layer without degradation, enabling reproducible metal halide memristors with reduced switching variation and significantly enhanced endurance relative to those based on a conventional thermally evaporated metal contact (EVC). Furthermore, the general applicability of vdWC approach is demonstrated by adopting various metal halide active layers, which ensures versatile utility of the vdWC for high performance memristive applications.

Formation of Intact van der Waals metal contacts

The memristors are fabricated based on solution processed hexagonal formamidinium lead triiodide (δ-$FAPbI_3$) thin films with structure of Si/Pt/$FAPbI_3$/Ag[24]. On top of the $FAPbI_3$ films, Ag metal contacts are formed by either conventional thermal evaporation (EVC) or physical lamination of the pre-deposited metal contacts through van der Waals force (vdWC) as depicted in **Fig. 1a**. Photographs of the devices based on the vdWC is shown in **Fig. 1b** where most of the vdWCs are successfully transferred onto the $FAPbI_3$ films. An optical microscopy image with the higher magnification in **Fig. 1c** confirms a well-defined Ag electrode array formed by the transfer process.

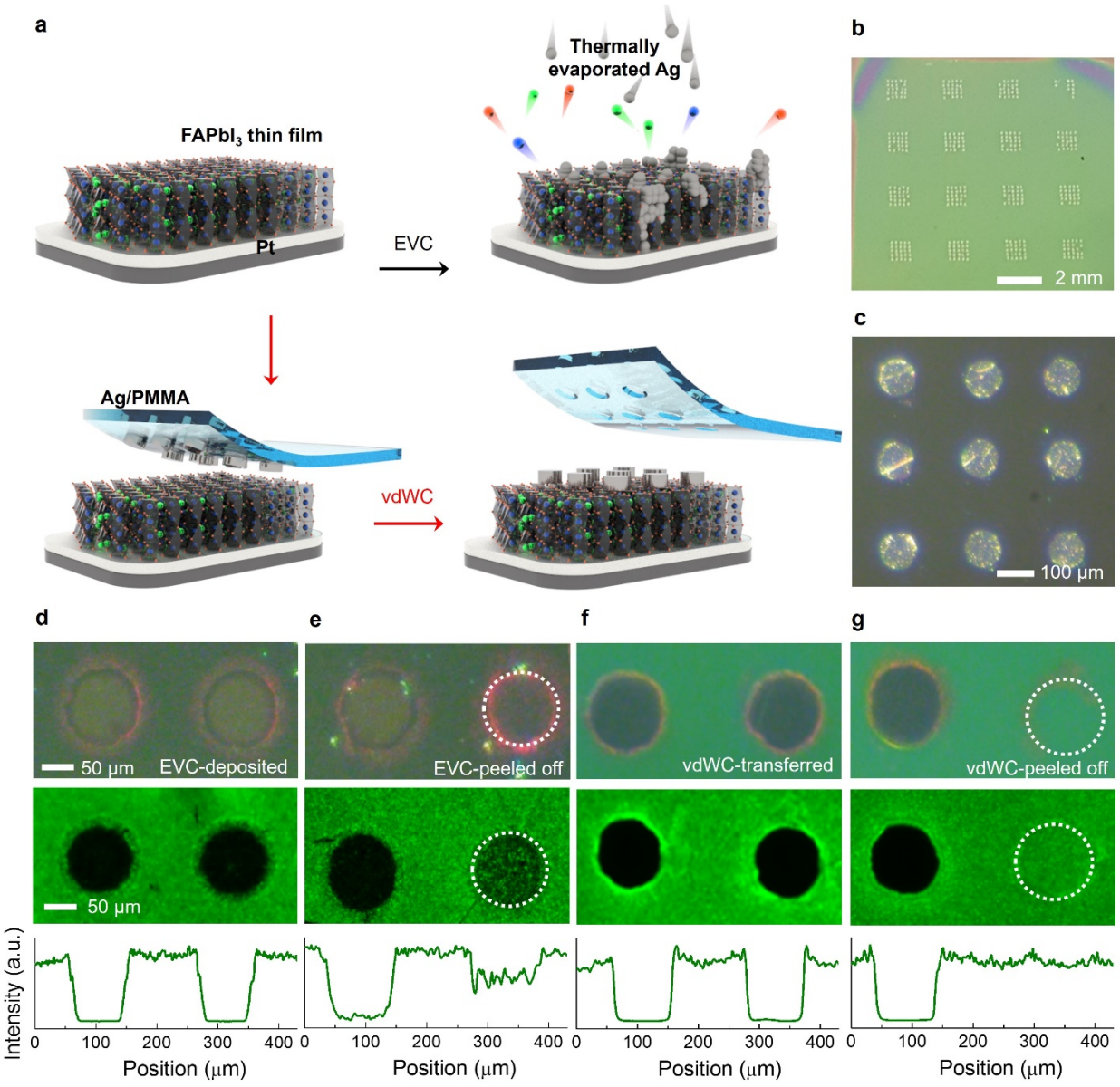

To investigate possible physical and chemical interactions between the metal contacts and underlying $FAPbI_3$ layer, optical microscopy (upper panels) and corresponding photoluminescence (PL) mapping images (middle panels) are measured in **Fig. 1d-g** where line scan of the PL intensity is

shown in the lower panels. The PL emission spectrum of the δ-$FAPbI_3$ film spans from around 650 nm to 900 nm (**Supplementary Fig. 1**), probably due to charge carrier funneling from δ-$FAPbI_3$ to trace α-$FAPbI_3$ in the film[25]. The PL mapping images are obtained before (**Fig. 1d**,**f**) and after peeling off the deposited metal contacts using adhesive tape (**Fig. 1e**,**g**). Before peeling off the metal contacts, the film region covered by EVC or vdWC is clearly visible as dark spots (middle panes of **Fig. 1d**,**f**). After the EVC is peeled-off, the PL intensity is notably lower in the region where the deposited EVC was located (the region enclosed with white dashed lines in **Fig. 1e**), compared to the region without metal contacts. This implies that EVC deposition process possibly degrades optoelectronic quality of the underlying $FAPbI_3$ films, resulting in non-radiative recombination[26]. On the contrary, after peeling off of the vdWC, the region where the vdWC was transferred showed comparable PL intensity with that of the region without metal contacts (**Fig. 1g**), indicating the $FAPbI_3$ layer under the vdWC remains intact.

Time-of-flight secondary-ion mass spectrometry (TOF-SIMS) is measured for studying depth distribution of deposited metal atom in the $FAPbI_3$ memristors (**Fig. 2a**,**b**). In the device with EVC, Ag atom seems to penetrate into the bulk $FAPbI_3$ layer, which makes the boundary between the Ag and $FAPbI_3$ layer unclear (**Fig. 2a**)[27]. In particular**,** relative intensity of Pb at the top electrode region is comparable to that of Ag, suggesting that severe physical and/or chemical interactions occur between the Ag and $FAPbI_3$ layers. It can be attributed to bombardment of the $FAPbI_3$ surface by the thermally excited metal atoms, which provides enough thermal and kinetic energy for the metal atoms to diffuse into and/or react with the underlying $FAPbI_3$ layer during the thermal evaporation process. For the devices with vdWC in **Fig. 2b,** Ag and $FAPbI_3$ layers were clearly distinguishable, indicating well-defined planar van der Waals heterojunction formed between the vdWC and $FAPbI_3$ layers.

To investigate possible changes in surface morphology and electrical properties of the underlying $FAPbI_3$ layer with different top metal contacts, conductive atomic force microscopy (c-AFM) images of bare $FAPbI_3$ film, and the $FAPbI_3$ films after peeling-off the EVC or vdWC (hereafter referred to as EVC-off and vdWC-off, respectively) are in comparison (**Fig. 2c**-**e**). Optical microscopy (upper panel), topography (middle panel) and c-AFM images (lower panel) are shown for each sample. The regions where metal contacts were peeled off are marked with red dashed lines in the optical microscopy images in **Fig. 2d**,**e**, and the regions highlighted with a black solid square are analyzed through the c-AFM measurement. Compared to the bare $FAPbI_3$ film (**Fig. 2c**), the EVC-off film shows significantly altered surface morphology and electrical characteristics (**Fig. 2d)**. The scanned images

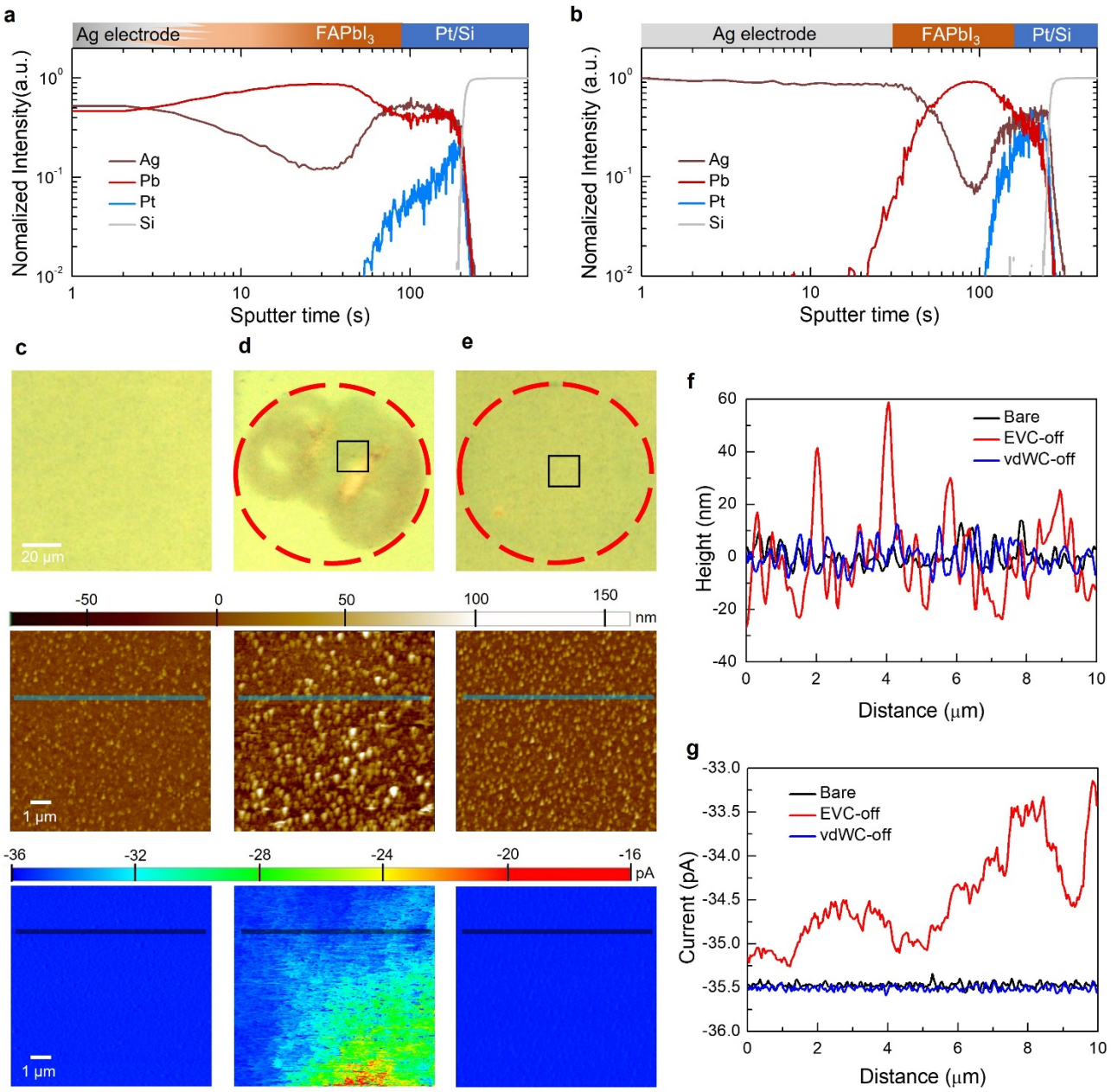

Fig. 2 | Topology and conductivity change by the metal contacts. **a,b,** Time-of-flight secondary ion mass spectroscopy (TOF-SIMS) profiles of the devices with structure of Si/Pt/$FAPbI_3$/Ag based on (**a**) EVC and (**b**) vdWC. **c-e,** Optical microscopy (upper panel), conductive atomic force microscopy (c-AFM, middle panel) and surface topography (lower panel) images of (**c**) a bare $FAPbI_3$ film, (**d**) the $FAPbI_3$ film after peeling off the EVC (EVC-off), (**e**) and vdWC (vdWC-off). **f,** Line scan profiles of topography at the region marked with blue lines on topography images. **g,** Line scan profiles of the c-AFM at the region marked with black lines on the c-AFM images.

show the increase in surface roughness and inhomogeneous conductivities of the EVC-off film, which is more evidently shown in the line scan profiles of the topography and conductivity in **Fig. 2f**,**g**. This might be due to residual Ag having chemical interactions with the $FAPbI_3$ layer and/or damaged

underlying $FAPbI_3$ layer during the thermal evaporation and the peeling-off process. The residual Ag on the $FAPbI_3$ film is detected by X-ray photoelectron spectroscopy (XPS) in **Supplementary Fig. 2**. A clear Ag 3d peaks are observed from the EVC-off film surface, and chemical shifts of the Pb 4f, I 3d and N 1s peaks relative to those in the bare film suggest that there are chemical interactions between the residual Ag and $FAPbI_3$ layer. The unintended chemical interactions between the EVC and $FAPbI_3$ layer can alter electrical and electronic properties of the $FAPbI_3$ layer, which hampers utilization of intrinsic properties of $FAPbI_3$. Indeed, ultraviolet photoelectron spectroscopy (UPS) data in **Supplementary Fig. 3** showed that position of energy band edges and fermi level for the EVC-off sample is altered from those measured in the bare $FAPbI_3$ film. For the region where the vdWC is peeled off, we identified that the $FAPbI_3$ film surface morphology and conductivity is almost unchanged compared to the bare $FAPbI_3$ film (**Fig. 2e-g**), which is consistent with the PL mapping data in **Fig. 1**.

Memristors based on van der Waals metal contacts

The current-voltage (*I-V*) curves of the $FAPbI_3$ memristors based on EVC and vdWC are shown in **Fig. 3a**,**b**, respectively. The bipolar resistive switching behavior is observed for both devices. When the first positive voltage sweep (0 V→0.6 V→0 V, compliance current of 10^{-3} A) is applied, resistance is changed from high resistance state (HRS) to low resistance state (LRS), which is a set process by forming the CFs. Upon application of negative voltage sweep (0 V→-0.6 V→0 V, compliance current of 10^{-1} A), a reset process occurs where resistance is changed from LRS to HRS by rupturing the CFs. For the device based on EVC, the CFs are formed at ~0.27 V, which is substantially lower than ~0.49 V for that based on vdWC. (black dashed lines in **Fig. 3a,b**). After the forming process, the next ten scans were conducted with the lower positive bias voltage (0 V→0.35 V→0 V→-0.6 V→0 V) but same compliance current. As shown in **Fig. 3a,** the device based on EVC showed comparable set voltages for the first forming scan and the next ten scans. On the contrary, there is clear difference in the set voltages for the first forming scan and the next ten scans for the vdWC device. The relatively lower forming voltage of the EVC device could be caused by thermally evaporated Ag atoms that penetrate and react with the $FAPbI_3$ layer, resulting in formation of unintended chemical bonding and relevant defects. The (reacted) Ag atoms in the $FAPbI_3$ layer reduces an activation energy for electrochemical metallization (ECM) and valence change of the $FAPbI_3$ layer and thus facilitates migration of Ag atoms and iodide vacancies at relatively lower bias voltage (**Supplementary Fig. 4a**). On the other hand, the vdWC hardly generates additional defects during the transfer process. Thus, the

Ag atom penetration at the well-defined van der Waals heterojunction in the vdWC device should require a relatively higher bias voltage than that in the EVC device (**Supplementary Fig. 4b**)[28,29], resulting in the higher forming voltage for the vdWC device than that for EVC one. During additional 10 scans, the average set voltages of EVC and vdWC devices were 0.18±0.048 and 0.17±0.029 V, respectively. The well-defined van der Waals junction between the vdWC and $FAPbI_3$ layer probably enables more reproducible formation of the CFs, and thus the narrower distribution of set voltages (**Supplementary Fig. 4**). For the case of reset voltages, the average and deviation for both devices were comparable (-0.22±0.042 and 0.19±0.049 V for EVC and vdWC devices, respectively). The comparable reset voltages indicate that the size and orientation of the formed CFs are similar, irrespective of the contact layer[30].

In **Fig. 3c**, time-resolved current decay curves, $I(t)$ are measured to estimate concentration of mobile ions (defects) in the EVC and vdWC devices. Since the total current is the sum of electronic current ($I_{electronic}$) and ionic current (I_{ionic}), the I_{ionic} was obtained by subtracting $I_{electronic}$ from the total current. While the $I_{electronic}$ can flow through the electrodes, the mobile ions accumulate at the interfaces between the $FAPbI_3$ layer and electrodes. As a result, the $I_{electronic}$ has a steady-state value (I_{ss}) whereas I_{ionic} is transient. Therefore, we estimated migrated mobile ion concentration using the equation[31-33] given by:

$$migrated\ ion\ concentation = \int_0^t I(t) - I_{ss}dt \times \frac{1}{volume\ of\ the\ perovskite\ layer}$$

The migrated ion concentration for each device is plotted in **Fig. 3c**. The lower total migrated ion concentration of vdWC device at given time suggests the mobile ionic defect density in the vdWC device is lower than that in EVC one. This supports the thermal evaporation process of the Ag metal contact generates additional defects in the underlying $FAPbI_3$ layer. It is also possible to speculate that the chemically reactive nature of the Ag atom with metal halides is the origin of the defects in the $FAPbI_3$ layer. We also compared the defect density of the EVC and vdWC devices based on non-reactive gold contact using space charge limited current (SCLC) measurement (**Supplementary Fig. 5**). Since we used the identical $FAPbI_3$ layer, the trap filling voltage (V_{TFL}) should be linearly proportional to the trap density in the film[34]. The average V_{TFL} of EVC devices (0.50±0.092 V) is about 1.6 times than that of vdWC one (0.31±0.083 V), indicating that trap density in the EVC device is about 1.6 times higher than that in the vdWC one. This indicates not only the reactive nature of the Ag

atom, but also physical damage by the thermally excited metal atoms causes the defects in the underlying $FAPbI_3$ layer during the thermal evaporation process.

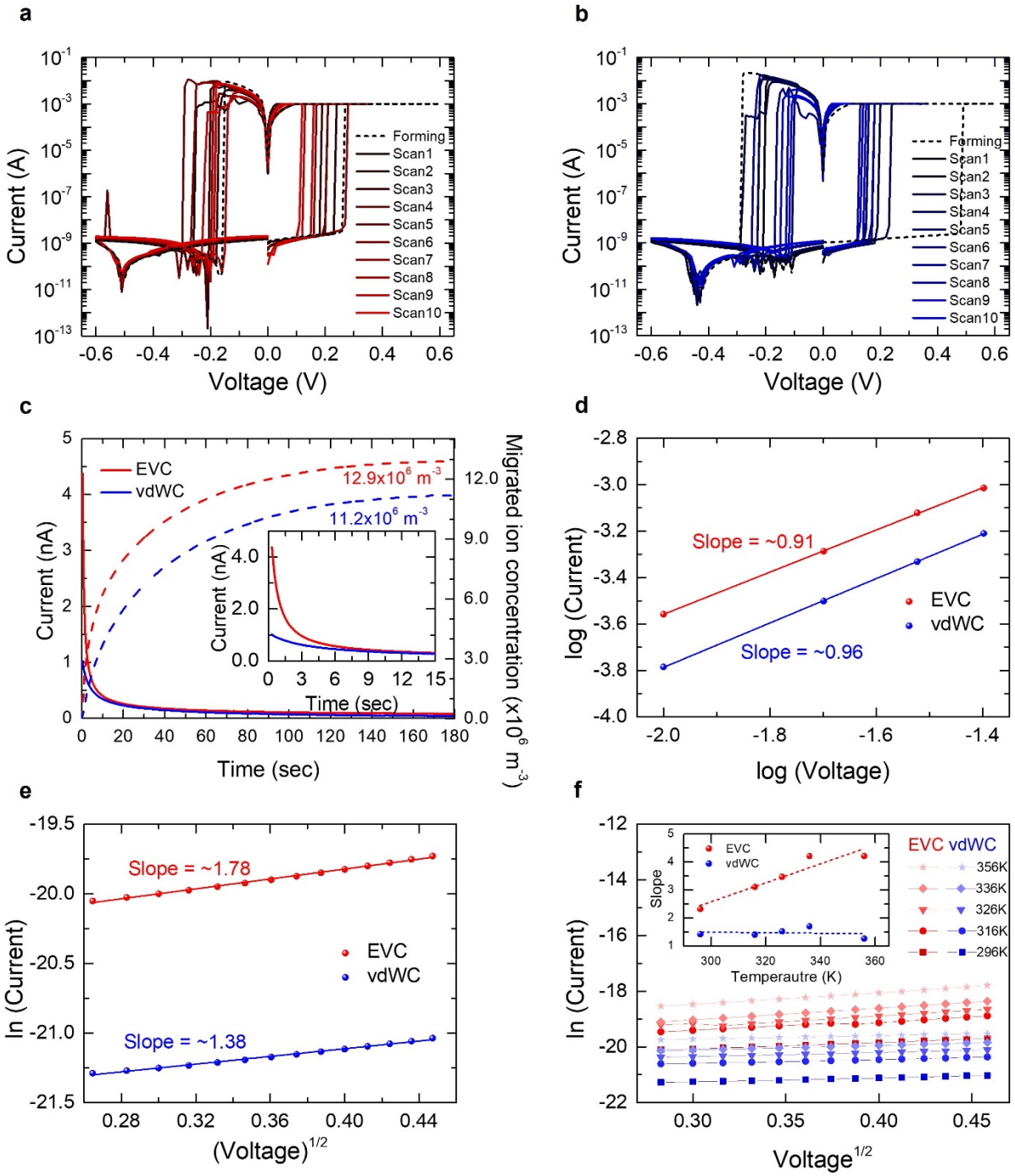

Fig. 3 | Electrical properties of memristors based on the EVC and vdWC. a,b, Current-voltage (*I-V*) characteristics of the memristors based on EVC (**a**) and vdWC (**b**). **c,** Time-resolved current decay curves and net migrated ion concentration within the devices measured with a DC bias voltage of 0.05 V. The inset shows magnified plots at the initial stage of the measurement. **d,** A log(*I*)-log(*V*) plot of the devices based on EVC and vdWC at low resistance state (LRS). **e,** A ln(*I*)-$V^{1/2}$ plot of the devices at high resistance state (HRS). The filled circles are measured data and solid lines are fitted lines. **f,**

The ln(I)-$V^{1/2}$ plots in the HRS measured at various temperature from 296 K to 356 K. The inset shows slopes of the plots as a function of temperature.

To study conduction mechanism in both devices, plots of log I-log V in LRS and ln I-$V^{1/2}$ in HRS are analyzed in **Fig. 3e**,**d**. In LRS, carrier transport mechanism of both EVC and vdWC devices is ohmic conduction as confirmed by linear relationship between the current and voltage. With a slope of 0.96, the vdWC forms more ideal ohmic junction with underlying $FAPbI_3$ than EVC dose (slope ~0.91, **Fig. 3d**). In HRS, the conduction mechanism for both devices was found to be Schottky emission as evidenced by a linear relationship between the ln I and $V^{1/2}$ (**Fig. 3e**)[35,36]. Interestingly, the slope of the plot for EVC is much lower than that of vdWC devices. The Schottky barrier is expected to be formed at the interface between the $FAPbI_3$ and Pt due to large workfunction difference. The Schottky emission equation is given by

$$I = A^{*}T^{2}exp\left[\frac{-q(\emptyset_B - \sqrt{qV/4\pi\varepsilon_r\varepsilon_0 d})}{kT}\right]$$

where I is the current, A^* is the effective Richardson constant, T is the absolute temperature, q is the electron charge, k is the Boltzman constant, $q\emptyset_B$ is the Schottky barrier height, V is the external voltage, ε_r is the optical dielectric constant, ε_0 is the permittivity in vacuum, and d is the Schottky barrier thickness[35,36]. According to the equation, the d is inversely proportional to the slope as $d \propto (\frac{1}{slope})^2$. Therefore, the d is thinner for the device based on the EVC than that based on vdWC. We speculate that the migrated ionic defects generated by the thermal evaporation in the EVC device might compensate for the built-in potential to decrease the Schottky barrier thickness in the EVC device. To further verify our speculation, the ln I-$V^{1/2}$ curves of the devices at different temperatures are investigated in **Fig. 3f**. Notable difference was found in temperature dependent slope change in the ln I-$V^{1/2}$ curves. While the slope is decreased as temperature increases for vdWC device, it was anomalously increased for the EVC device. We attributed the anomalous increase in the slope and thus reduced barrier thickness with increasing temperature to the heat induced activation of the defect migration pronounced in the EVC device. For both devices, the linear relationship between ln(I/T^2) and 1000/T is observed with different bias voltages from 0.05 V to 0.15 V (**Supplementary Fig. 6**), which confirms the Schottky emission conduction in HRS of both EVC and vdWC devices.

In **Fig. 4**, resistive memory operation reproducibility of the devices based on the EVC and vdWC is compared. For each condition, the histograms for operating voltages of 350 devices on 7 substrates fabricated in the same batch are shown in **Fig. 4a-c**. Consistent with the data in **Fig. 3a**,**b**, an average forming voltage for vdWC devices is 0.36±0.049 V, higher than 0.27±0.051 V of EVC

one (**Fig. 4a** and **Supplementary Table 1**). In the histogram of set voltage, the vdWC device (0.16±0.036 V) has relatively narrower distribution than the EVC device (0.19±0.050 V, **Fig. 4b**). The relatively poor reproducibility of the EVC device was observed from the device to the other devices in the same substrate as well as from the substrate to the other substrate. The position dependent evaporation rate and thus energy of the Ag atom probably causes penetration and reaction of the Ag atom in the underlying $FAPbI_3$ layer to a varying degree to cause such wide distribution in set voltage. Thus, the vdWC device, free from such damage, shows relatively uniform junction and thus operating voltage.

The HRS and LRS resistances of the 350 cells for both EVC and vdWC devices are demonstrated in **Fig. 4d**,**e**. The average LRS and HRS resistances of the EVC device are 109.2±44.3 Ω and $1.52\times10^8\pm1.52\times10^8$ Ω, respectively (**Fig. 4d**) while those of the vdWC devices are 69.4±34.8 Ω and $5.4\times10^7\pm2.6\times10^7$ Ω, respectively (**Fig. 4e**). The formation of reproducible van der Waals heterojunction without generating additional defects during the fabrication process could be the origin of much narrower distribution of the LRS and HRS resistances of the vdWC device than those of EVC one. It is noted that a quite large proportion of the EVC devices suffer from serious reaction between the EVC and $FAPbI_3$ layer and those devices show anomalously higher resistance (lower current) than EVC devices with less reaction and vdWC devices, probably due to the increase in series resistance of degraded metal contact and formation of insulating AgI_x layer (**Supplementary Fig. 7**). Especially in HRS without the CFs, the conductance was largely decreased. To investigate batch reproducibility, the box plot for set and reset voltages of the devices from 3 different batches are presented in **Fig. 4f** (the box plot for forming voltage of the devices is shown in **Supplementary Fig. 8**). As summarized in **Supplementary Tables 2-4**, the vdWC devices fabricated in the different batch have relatively less operating deviation, especially for the set voltage compared to the EVC devices.

On/off switching cycle endurance of the devices is tested in **Fig. 5a**. While the EVC device failed after ~650 cycles of operation, the vdWC device remained operable up to 2100 cycles, more than 3-fold improvement in endurance. The major reset failure that has been reported is likely due to formation of permanent conducting filaments involving a large amount of metal atoms or anion vacancies[37,38]. When the voltage is applied, the Ag atoms in the EVC can easily migrate into the $FAPbI_3$ layer through chemical bonding to participate in forming the CFs. As the number of the operation cycles increases, the more migration of metal atoms can occur[39,40]. At the end, permanent metal filaments that cannot be ruptured cause the failure of switching in the EVC devices. In this regard, the dramatically improved endurance of the vdWC device is owing to the well-defined van der Waals

heterojunction with the relatively higher activation energy for Ag atom penetration to prevent formation of the permanent CFs.

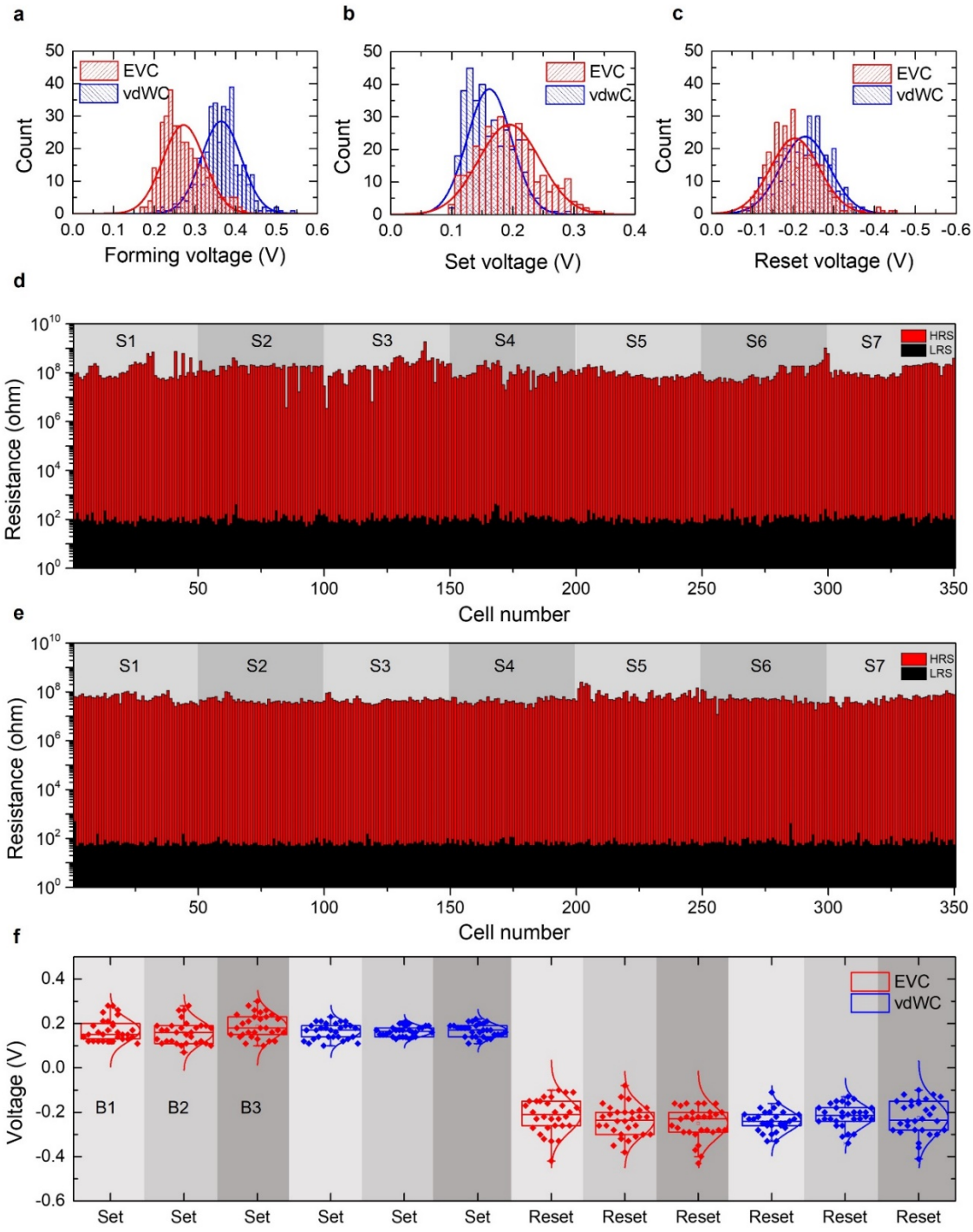

Fig. 4 | Statistical operation property analysis. a-c, Operating voltage of the 350 devices based on EVC and vdWC in the same batch; forming voltage (**a**), set voltage (**b**), reset voltage (**c**). **d,e,** On/off ratio of 350 devices on 7 substrates (denoted as S1, S2, ..., S7) based on the EVC (**d**) and vdWC (**e**) in the same batch, **f,** A box plot for operating voltages of the 30 devices based on EVC and vdWC fabricated in three different batches.

To evaluate storage stability, the *I-V* characteristics of the devices were tracked for 30 days (**Fig. 5b**,**c**). The vdWC device retained relatively more consistent *I-V* characteristics than that of EVC device. After 10 days, the HRS resistance of the EVC device sharply increased, which can be attributed to the aforementioned reaction of the EVC with $FAPbI_3$ layer. The relatively severe reaction between the EVC and $FAPbI_3$ layer was confirmed in X-ray diffraction (XRD) measurement where appearance of a AgI peak with higher intensity is observed for the EVC device (**Supplementary Fig. 9**). Optical microscopy images in **Supplementary Fig. 10** further show more reactive interaction between the EVC and $FAPbI_3$ layer than vdWC. The insulating AgI formation might cause the increase in series resistance and thus alteration in distribution of applied electric field as well as generation of additional defects[41]. All these factors could affect the operation characteristics of the EVC device to degrade device reliability. Temperature-dependent *I-V* characteristics of both devices are measured for studying the thermal stability (**Fig. 5d**,**e**). In the vdWC devices, relatively more stable set/reset operation is observed across all the temperature tested whereas incomplete reset of EVC device occurred at 356 K. As temperature increases, the migration of Ag atom and its reaction with other defects in EVC might be further promoted to generate the permanent CFs which induce the incomplete reset of the device.[42]. We observed that the device with more serious reaction between the EVC and $FAPbI_3$ layer suffers from relatively poor thermal stability. In other word, a few EVC devices with relatively less reaction between the EVC and $FAPbI_3$ layer showed better thermal stability (**Supplementary Fig. 11**), supporting detrimental effects of the damage caused by the direct deposition on thermal stability of the devices. Similar to the operation characteristics, such various thermal stability of the EVC devices was observed from device to device in the same substrate as well as from substrate to substrate. Retention capability with on/off ratio higher than 10^7 was confirmed for the vdWC devices with reading voltage 0.05 V (**Supplementary Fig. 12).** The multi-level storage ability for the vdWC devices was also demonstrated with the different compliance current levels from 1 mA to 0.01 mA (**Supplementary Fig. 13)** with retention time for 1000 s.

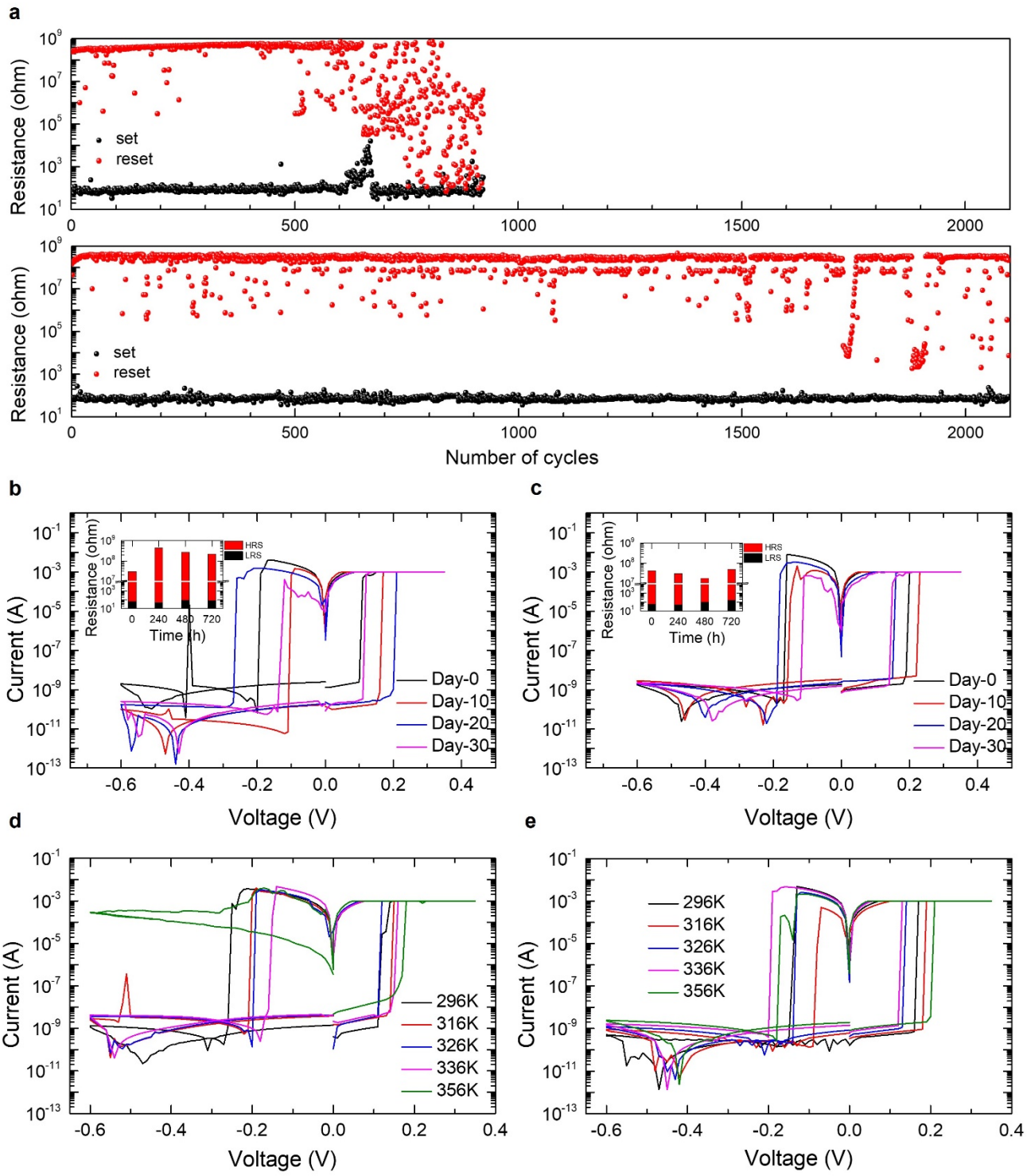

Fig. 5 | Stability of the memristors. a, The endurance measurement of Si/Pt/$FAPbI_3$/Ag devices based on EVC (upper panel) and vdWC (lower panel). Applied voltage pulses= 0.25 V, pulse width = 640 μs, compliance current (CC) = 1 mA for set and applied voltage pulses= -0.42 V, pulse width = 1 ms, CC = 100 mA for reset, reading voltage = 0.03 V. **b,c,** Time-dependent current-voltage (I-V) characteristics of the devices measured for 30 days(inset: HRS and LRS resistance values of the devices with different aging time). **d,e,** The I-V characteristics of the devices measured at different temperature. EVC device (**b,d**) and vdWC device (**c,e**).

Universal application of van der Waals metal contacts

To confirm that the proposed vdWC approach is universally applicable, memristor devices based on different active materials are tested in **Fig. 6**. *I-V* characteristics of the EVC and vdWC devices based on 2D $(PEA)_2PbI_4$ perovskite are measured in **Fig. 6a**,**b**. Similar to the $FAPbI_3$ memristor devices, the vdWC based $(PEA)_2PbI_4$ memristor device showed relatively higher forming voltage (~0.35 V) than that of EVC one (~0.21 V), indicating well-defined van der Waals heterojunction between the vdWC and $(PEA)_2PbI$ layer. Also, the device based on vdWC demonstrates higher HRS resistance and narrower distribution of set/reset voltages. These results can be attributed to more well-defined van der Waals heterojunction between the vdWC and $(PEA)_2PbI_4$ layer without generation of additional defects. The poor junction between the EVC and $(PEA)_2PbI_4$ layer might be the origin of larger operating voltage deviation and the lower HRS resistance of the EVC device. In particular, the EVC device shows gradual reset characteristics with higher reset voltage, which was attributed to the higher defect concentration as well as lower activation energy for Ag atom penetration, making the CFs harder to rupture[30]. In **Fig. 6c,d**, operation endurance of the devices was examined. As expected, well-defined vdWC enabled significantly improved endurance performance of the vdWC devices (~350 cycles) relative to the EVC devices (~170 cycles).

We further adopted lead-free all-inorganic $Cs_3Cu_2I_5$ perovskite for fabrication of EVC and vdWC devices (**Fig. 6e**,**f**). In the forming *I-V* scan, the distinct dual switching characteristic is observed for both EVC and vdWC devices, in which charge trapping and ion migration enabled switching are involved[43,44]. In **Supplementary Fig. 14**, carrier conduction mechanism at two different LRS states (LRS1 and LRS2) are investigated. With ohmic/sub-ohmic behavior at HRS, the switching from the HRS to LRS1 seems to involve transition from the ohmic to trap-free SCLC region[43,44]. In this region, we can identify that the V_{TFL} of EVC device is higher than vdWC one, suggesting that EVC device has higher defect density than vdWC one. Upon applying the higher bias voltage, second transition from LRS1 to LRS2 occurred by forming the CFs[43,44]. In this case, different from $FAPbI_3$ and $(PEA)_2PbI_4$ devices based on filamentary only switching, the forming voltage for EVC device was rather higher than vdWC one, which might be due to association of different switching mechanisms. After the forming step, the switching was observed only in the filamentary conduction region. In the case of EVC device, HRS/LRS switching characteristics is gradually degraded as increasing the number of voltage scan (**Fig. 6e**). The HRS and LRS are not reproducible but fluctuated with lower on/off ratio than vdWC device. The vdWC device shows relatively less switching variation and maintains higher

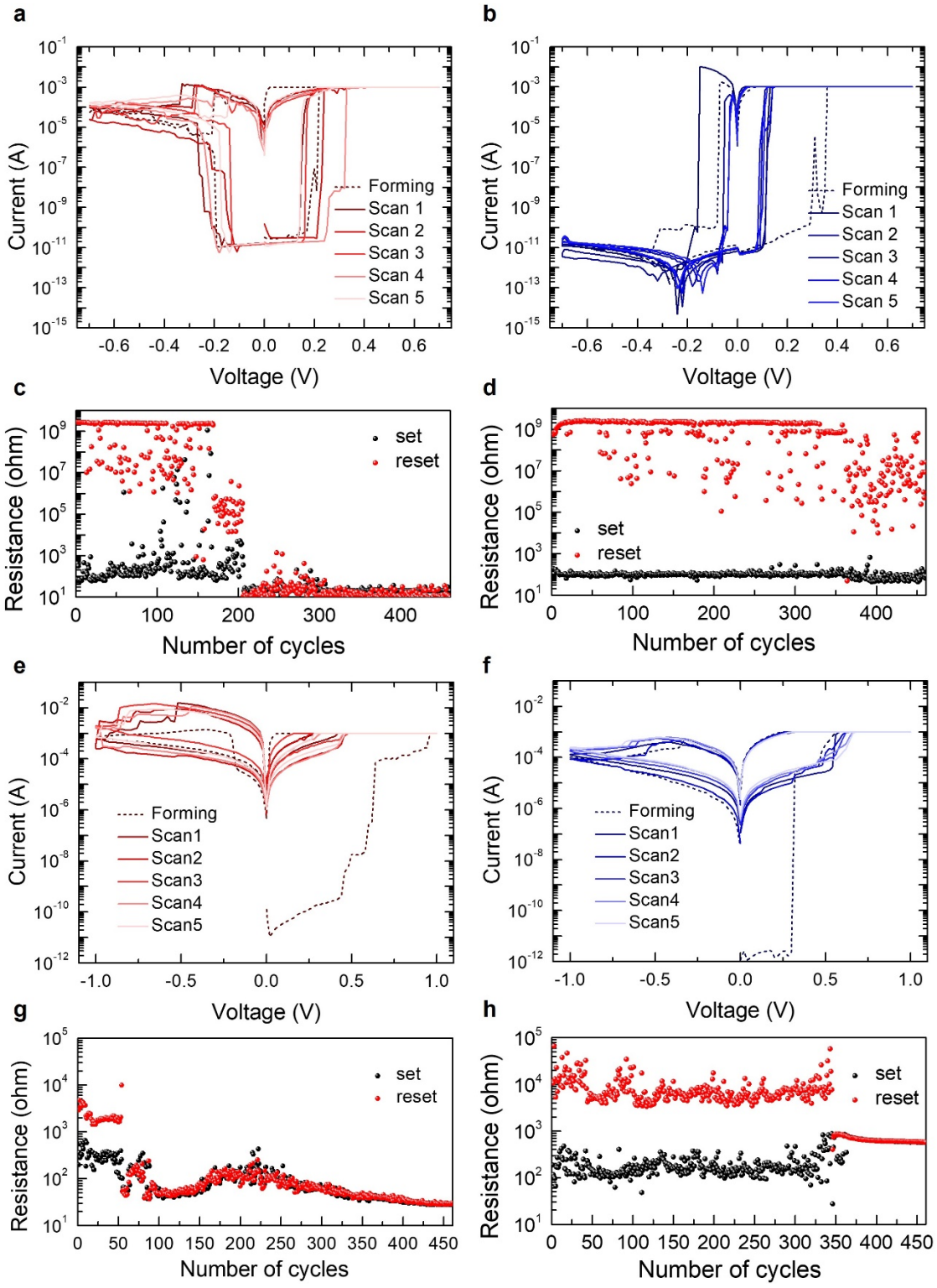

Fig. 6 | Various metal halide memristors. a,b, Current-voltage (I-V) characteristics of Si/Pt/$(PEA)_2PbI_4$/Ag devices based on EVC (**a**) and vdWC (**b**). **c,d,** Endurance measurements of the devices based on EVC (**c**) and vdWC (**d**). **e,f,** The I-V characteristics of ITO/$Cs_3Cu_2I_5$/Ag devices based on EVC (**e**) and vdWC (**f**). **g,h,** Endurance measurements of the devices based on EVC (**g**) and vdWC (**h**).

on/off ratio with consecutive voltage sweeps (**Fig. 6f**). Endurance performance of the devices is shown in **Fig. 6g**,**h**. Consistent with $FAPbI_3$ and $(PEA)_2PbI_4$ memristor device results, endurance of vdWC device is significantly enhanced to >325 cycles relative to <50 cycles of the EVC device with superior on/off ratio. These results confirm that vdWC approach is universally applicable to memristors with various metal halide compositions despite having different switching mechanisms.

Conclusions

We have reported the vdWC approach to fabricate high-performance and reliable memristors based on metal halide materials. Physical lamination of pre-deposited metal contacts onto the active layer enabled formation of a well-defined and reproducible van der Waals heterojunction without generating unintended physical and chemical interactions between the metal contacts and active layer that has been found between the conventional EVC and underlying active layer. Consequently, while retaining high optoelectronic quality of the active layer, the vdWC enables less switching variation of metal halide memristors and significant enhancement in endurance and reproducibility, compared to those of the devices based on the EVC. The vdWC approach was found to be universally applicable to fabricate memristors based on various active layer compositions despite having different switching mechanisms. We believe this study provides a promising platform technology for development of high-performance and reliable memristors for future computing.

Methods

Fabrication of metal halide active layers.

Fabrication of $FAPbI_3$ thin film. The 35 wt% of $FAPbI_3$ precursor solution was prepared by dissolving 1mmol of FAI (172 mg, 99.99%, Greatcell Solar), 1 mmol of PbI_2 (461 mg, 99.99%, TCI), and 1 mmol of N-Methyl-2-pyrrolidone (NMP, 99.1 mg, 99.5%, Sigma-Aldrich) in 1080 mg of N,N-dimethylformamide (DMF, 99.8%, Sigma-Aldrich). The precursor solution was filtered by a 0.2 μm PTFE-H filter before use. The precursor solution was spin coated on the cleaned Pt-coated Si wafer at 4000 rpm for 30 s to which 0.2 mL of diethyl ether (>99.7%, Sigma-Aldrich) was poured after 20 s of the spinning. The as-spun film was annealed on a hot plate at 110 °C for 10 min.

Fabrication of PEA_2PbI_4 thin film. The 0.5 M PEA_2PbI_4 perovskite solution was prepared by dissolving 2 mmol of phenethylammonium iodide (PEAI, 498 mg) (>99%, Greatcell Solar), and 1 mmol of PbI_2 (461 mg, 99.99%, TCI) in 0.2 mL of DMF. The precursor solution was filtered by a 0.2 μm PTFE-H filter before use. The precursor solution was spin coated on the cleaned Pt substrate at 4000 rpm for

60 s. On the spinning substrate, the 0.3 mL of toluene (99.8%, anhydrous, Sigma Aldrich) was dropped after 48 s. The as-spun film was annealed at 75 °C for 30 min on the hot plate.

Fabrication of $Cs_3Cu_2I_5$ thin film. The 0.5 M of $Cs_3Cu_2I_5$ perovskite solution was prepared by dissolving 1.8 mmol of cesium iodide (CsI, 467 mg, 99.999%, Sigma-Aldrich), and 1.2 mmol of copper iodide (CuI, 228 mg, 99.999%, Sigma-Aldrich) in 1.2 mL of dimethyl sulfoxide (DMSO, anhydrous, >99.9%, Sigma-Aldrich). The precursor solution was filtered by a 0.2 μm PTFE-H filter before use. The precursor solution was spin coated on the cleaned ITO substrate at 4000 rpm for 30 s to which 0.2 mL of diethyl ether (>99.7%, Sigma-Aldrich) was poured after 20 s of the spinning. The as-spun films was annealed on the hot plate at 100 °C for 10 min.

Metal contact fabrication. For deposition of the vdWC, the metal contacts are pre-deposited on a Si wafer. The Si wafer was cleaned by successive sonication in detergent, acetone, and ethanol baths. On the cleaned Si wafer, a 100 nm-thick Ag or Au was deposited by electron-beam evaporation where patterned metal shadow mask is used. The metal contact deposited Si wafer was post-treated with a hexamethyldisilazane (HMDS, 99%, Sigma Aldrich). Specifically, the Si wafer was put in the glass bottle containing the 3 ml of HMDS, and the sealed bottle was heated at 120 °C for 30 min. The HMDS-treated Si wafer was washed with isopropanol and dried at 80 °C. Subsequently, polymethyl methacrylate (PMMA, Micro Chem, 495PMMA A8) solution was spin coated at 2000 rpm for 40 s, followed by annealing on hot plate at 180 °C for 10 min. The Au or Ag/PMMA layer was exfoliated by thermal release tape and attached on the active layer film surface. Since the HMDS-functionalized metal contacts have a weak interaction with the PMMA overlayer, it can be easily released from the PMMA by van der Waals interaction with a targeting layer. To enhance the adhesion of the transferred layer, 30 μl of chloroform (>99%, Sigma Aldrich) was dropped on the active layer film surface prior to the transfer. After the transfer, the film was heated at 90 ºC for few seconds to remove the thermal release tape. Finally, the remaining PMMA layer was removed by using chloroform. For the formation of EVC, the 100 nm-thick Ag or Au layer was directly deposited on the active layer films by thermal evaporation under 2.0×10^{-6} torr with deposition speed of 0.1-0.3 Å/s.

Steady-state PL and PL microscope characterization. Steady-state PL spectra were measured by a spectrometer equipped with a 464 nm excitation laser source (Hamamatsu Quantaurus-Tau C11367-12). The PL mapping images were collected by customized PL microscope, consists of microscopy (Zeiss Axio Imager.A2m), external LED light source (CoolLED pE-300 Lite Light source), and CCD camera (Andor Technology Zyla5.5) with light filter setup (Chroma Technology 19008-AT-Auramine

Longpass) to irradiate excitation light of 440 nm blue light. The excitation light intensity was adjusted to 65 mW/cm^2 with exposure time of 200 ms.

TOF-SIMS and AFM/c-AFM measurements. Time-of-flight secondary ion mass spectroscopy (TOF-SIMS) data were obtained by TOF-SIMS-5 (ION-TOF) using a 1 keV oxygen-ion beam sputter gun and 25 keV Bi^+ primary ion beam. The local topology and conductivity were investigated using a conductive atomic force microscopy (C-AFM, Park Systems, NX10) at the contact mode under N_2 atmosphere with glovebox cage system (Mbraun, MB10 Compact).

XRD and XPS/UPS measurements. X-ray diffraction (XRD) patterns were measured by an X-ray diffractometer (Rigaku Smartlab SE) with Cu Kα radiation (λ = 1.5406 Å). The X-ray photoelectron spectroscopy (XPS) and Ultraviolet photoelectron spectroscopy (UPS) spectra were collected using a Thermo Fisher ESCALAB250 surface analysis system with micro-focused Al Kα X-ray for XPS and a He I discharge UV lamp (21.21 eV) for UPS.

Electrical measurements. The current-voltage characteristics of the devices were measured by a probe station equipped with a Keithley 4200 under moderate vacuum (~10^{-2} torr).

Data availability

The data that support the plots within this paper and other findings of the study are available from the corresponding author upon reasonable request.

References

1. Pan, F., Gao, S., Chen, C., Song, C. & Zeng, F. Recent progress in resistive random access memories: Materials, switching mechanisms, and performance. *Mater. Sci. Eng. R Rep.* **83**, 1-59 (2014).
2. Choi, S. *et al.* SiGe epitaxial memory for neuromorphic computing with reproducible high performance based on engineered dislocations. *Nat. Mater.* **17**, 335-340 (2018).
3. Sun, W. *et al.* Understanding memristive switching via in situ characterization and device modeling. *Nat. Commun.* **10**, 3453 (2019).
4. Jo, S. H. *et al.* Nanoscale Memristor Device as Synapse in Neuromorphic Systems. *Nano Lett.* **10**, 1297-1301 (2010).
5. Han, X. *et al.* Total Ionizing Dose Effects on Multistate HfO_x-Based RRAM Synaptic Array. *IEEE Trans. Nucl. Sci.* **68**, 756-761 (2021).
6. Yang, J. J., Strukov, D. B. & Stewart, D. R. Memristive devices for computing. *Nat. Nanotech.* **8**, 13-24 (2013).

7. Choi, J. *et al.* Organolead Halide Perovskites for Low Operating Voltage Multilevel Resistive Switching. *Adv. Mater.* **28**, 6562-6567 (2016).
8. Choi, J. *et al.* Enhanced Endurance Organolead Halide Perovskite Resistive Switching Memories Operable under an Extremely Low Bending Radius. *ACS App. Mater. Interfaces* **9**, 30764-30771 (2017).
9. Hwang, B. & Lee, J.-S. A Strategy to Design High-Density Nanoscale Devices utilizing Vapor Deposition of Metal Halide Perovskite Materials. *Adv. Mater.* **29**, 1701048 (2017).
10. Gu, C. & Lee, J.-S. Flexible Hybrid Organic–Inorganic Perovskite Memory. *ACS Nano* **10**, 5413-5418 (2016).
11. Xiao, X. *et al.* Recent Advances in Halide Perovskite Memristors: Materials, Structures, Mechanisms, and Applications. *Adv. Mater. Tech.* **5**, 1900914 (2020).
12. Cottrell, T. L. The strengths of chemical bonds. (1958).
13. Pedley, J. B. & Marshall, E. M. Thermochemical Data for Gaseous Monoxides. *J. Phys. Chem. Ref. Data* **12**, 967-1031 (1983).
14. Sorensen, J. J. *et al.* Bond dissociation energies of transition metal oxides: CrO, MoO, RuO, and RhO. *J. Chem. Phys.* **153**, 074303 (2020).
15. Reddy, R. R. *et al.* Spectroscopic Studies on Astrophysically Interesting TaO TaS, ZrS and SiO^{+} Molecules. *Astrophys. Space Sci.* **281**, 729-741 (2002).
16. Naulin, C., Hedgecock, I. M. & Costes, M. The dissociation energy of TiO determined from a crossed-beam study of the Ti + NO → TiO + N reaction. *Chem. Phys. Lett.* **266**, 335-341 (1997).
17. Ren, Y. *et al.* Cycling-Induced Degradation of Organic–Inorganic Perovskite-Based Resistive Switching Memory. *Adv. Mater. Tech.* **4**, 1800238 (2019).
18. Shan, Y. *et al.* Solution-processed resistive switching memory devices based on hybrid organic-inorganic materials and composites. *Phys. Chem. Chem. Phys.* **20**, 23837-23846 (2018).
19. Haick, H., Ambrico, M., Ghabboun, J., Ligonzo, T. & Cahen, D. Contacting organic molecules by metal evaporation. *Phys. Chem. Chem. Phys.* **6**, 4538-4541 (2004).
20. Liu, L. *et al.* Transferred van der Waals metal electrodes for sub-1-nm MoS2 vertical transistors. *Nat. Electron.* **4**, 342-347 (2021).
21. Liu, Y. *et al.* Approaching the Schottky–Mott limit in van der Waals metal–semiconductor junctions. *Nature* **557**, 696-700 (2018).
22. Saidi, W. A. Influence of strain and metal thickness on metal-MoS2 contacts. *J. Chem. Phys.* **141**, 094707 (2014).

23. Tung, R. T. Chemical Bonding and Fermi Level Pinning at Metal-Semiconductor Interfaces. *Phys. Rev. Lett.* **84**, 6078-6081 (2000).
24. Yang, J.-M. *et al.* 1D Hexagonal HC(NH2)2PbI3 for Multilevel Resistive Switching Nonvolatile Memory. *Adv. Electron. Mater.* **4**, 1800190 (2018).
25. Lee, D.-K. *et al.* Nanocrystalline Polymorphic Energy Funnels for Efficient and Stable Perovskite Light-Emitting Diodes. *ACS Energy Lett.* **6**, 1821-1830 (2021).
26. Wang, Y. *et al.* Probing photoelectrical transport in lead halide perovskites with van der Waals contacts. *Nat. Nanotech.* **15**, 768-775 (2020).
27. Zhang, T. *et al.* Profiling the organic cation-dependent degradation of organolead halide perovskite solar cells. *J. Mater. Chem. A* **5**, 1103-1111 (2017).
28. Cao, X. *et al.* Forming-free colossal resistive switching effect in rare-earth-oxide Gd_2O_3 films for memristor applications. *J. Appl. Phys.* **106**, 073723 (2009).
29. Hsiung, C.-P. *et al.* Resistance Switching Characteristics of TiO_2 Thin Films Prepared with Reactive Sputtering. *Electrochem. Solid-State Lett.* **12**, G31 (2009).
30. Park, K. & Lee, J.-S. Reliable resistive switching memory based on oxygen-vacancy-controlled bilayer structures. *RSC Adv.* **6**, 21736-21741 (2016).
31. Birkhold, S. T. *et al.* Interplay of Mobile Ions and Injected Carriers Creates Recombination Centers in Metal Halide Perovskites under Bias. *ACS Energy Lett.* **3**, 1279-1286 (2018).
32. Li, C. *et al.* Real-Time Observation of Iodide Ion Migration in Methylammonium Lead Halide Perovskites. *Small* **13**, 1701711 (2017).
33. Kang, D.-H., Kim, S.-Y., Lee, J.-W. & Park, N.-G. Efficient surface passivation of perovskite films by a post-treatment method with a minimal dose. *J. Mater. Chem. A* **9**, 3441-3450 (2021).
34. Zhao, Y. *et al.* Molecular interaction regulates the performance and longevity of defect passivation for metal halide perovskite solar cells. *J. Am. Chem. Soc.* **142**, 20071-20079 (2020).
35. Luo, Q. *et al.* Self-Rectifying and Forming-Free Resistive-Switching Device for Embedded Memory Application. *IEEE Electron Device Lett.* **39**, 664-667 (2018).
36. Chiu, F.-C. A Review on Conduction Mechanisms in Dielectric Films. *Adv. Mater. Sci. Eng.* **2014**, 578168 (2014).
37. Zhao, M. *et al.* Endurance and Retention Degradation of Intermediate Levels in Filamentary Analog RRAM. *IEEE J. Electron Devices Soc.* **7**, 1239-1247 (2019).
38. Lv, H. *et al.* Evolution of conductive filament and its impact on reliability issues in oxide-electrolyte based resistive random access memory. *Sci. Rep.* **5**, 7764 (2015).

39. Yuan, F., Zhang, Z., Pan, L. & Xu, J. A Combined Modulation of Set Current With Reset Voltage to Achieve 2-bit/cell Performance for Filament-Based RRAM. *IEEE J. Electron Devices Soc.* **2**, 154-157 (2014).
40. Min, K., Jung, D. & Kwon, Y. Investigation of switching uniformity in resistive memory via finite element simulation of conductive-filament formation. *Sci. Rep.* **11**, 2447 (2021).
41. Zeng, F. *et al.* Opportunity of the Lead-Free All-Inorganic $Cs_3Cu_2I_5$ Perovskite Film for Memristor and Neuromorphic Computing Applications. *ACS App. Mater. Interfaces* **12**, 23094-23101 (2020).
42. Celano, U. *et al.* Understanding the Dual Nature of the Filament Dissolution in Conductive Bridging Devices. *J. Phys. Chem. Lett.* **6**, 1919-1924 (2015).
43. Murgunde, B. K. & Rabinal, M. K. Solution processed bilayer junction of silk fibroin and semiconductor quantum dots as multilevel memristor devices. *Org. Electron.* **48**, 276-284 (2017).
44. Cheng, X.-F. *et al.* Pseudohalide-Induced 2D $(CH_3NH_3)_2PbI_2(SCN)_2$ Perovskite for Ternary Resistive Memory with High Performance. *Small* **14**, 1703667 (2018).

Acknowledgements

This work was supported by the National Research Foundation of Korea (NRF) grant funded by the Korea government (MSIT) under contract number 2020R1F1A1056938. This research was performed while S.-J.L. held an American Society for Engineering Education fellowship at NRL.

Author contribution

J-W.L. conceived an idea, supervised overall project, and prepared manuscript with help of N.-G.P., S-J.L. and J.-H.L. J-H.L. performed most of the experiment including fabrication and characterization of devices and collection of XRD, PL mapping, TOF-SIMS, XPS/UPS data. J-M.Y. and N-G.P. assisted in device characterization. S-Y.K. performed c-AFM measurements. S.B. and S.L. carried out electron beam deposition. All authors discussed the results and commented on the manuscript.

Competing interests

The authors declare no competing interests.

Additional Information

Supplementary information

Correspondence and requests for materials should be addressed to J-W.L.

Peer review information

Reprints and permissions information is available at www.nature.com/reprints.

Publisher's note Springer Nature remains neutral with regard to jurisdictional claims in published maps and institutional affiliations.

Supplementary Files

This is a list of supplementary files associated with this preprint. Click to download.

- FinalSIforvdWC.docx